Yun, X., Gardner, L. and Boissonnade, N. (2018) Ultimate capacity of I-sections under combined loading – Part 1: Experiments and FE model validation. Journal of Constructional Steel Research, **147**, 408-421.

Ultimate capacity of I-sections under combined loading – Part 1: Experiments and FE model validation

Xiang Yun [a], Leroy Gardner [b], Nicolas Boissonnade [c]

[a] Department of Civil and Environmental Engineering, Imperial College London, SW7 2AZ, UK.

Email: x.yun14@imperial.ac.uk

[b] Department of Civil and Environmental Engineering, Imperial College London, SW7 2AZ, UK.

Email: leroy.gardner@imperial.ac.uk (Corresponding author)

[c] Department of Civil and Water Engineering, Laval University, Quebec, Canada

Email: nicolas.boissonnade@gci.ulaval.ca

Abstract

An experimental and numerical study of hot-rolled steel I-sections under combined compression and bending moment is presented herein. A total of two stub column tests and 12 mono-axial or bi-axial eccentric compression tests on HEB 160 cross-sections with two different material grades (S235 and S355) were carried out. The tested cross-sections were of stocky proportions to enable the influence of material strain hardening on the strength and behaviour of hot-rolled steel I-sections to be investigated. The loading eccentricities for the eccentric compression tests were varied in order to achieve different axial compression-to-bending moment ratios. Measured geometric and material properties, together with the full load-deformation histories from the test specimens, were reported. Finite element (FE) models were developed and validated against the experimentally obtained load-deformation curves, as well as the failure modes. The FE results successfully captured the experimental structural performance of hot-rolled steel I-sections and the validated FE models were then used for parametric studies in the companion paper to generate additional numerical results, considering different cross-section slendernesses, material grades and combinations of loading. The experimental and numerical results are employed in the companion paper for the assessment of the design rules given in EN 1993-1-1 (2005) and AISC-360-16 (2016) and for the extension of the deformation-based continuous strength method to the case of hot-rolled steel I-sections under combined loading.

Keywords: Combined loading, Cross-sectional behaviour, Experimental investigation, Hot-rolled steel I-sections, Numerical models, Strain hardening

1. Introduction

Hot-rolled steel I-sections are generally the product of choice in structural frameworks, and have been extensively studied for many years. In terms of determining their structural design resistances, the concept of cross-section classification is used in current design codes, e.g. EN 1993-1-1 [1] and AISC-360-16 [2], where four classes of cross-section – Class 1 (plastic), Class 2 (compact), Class 3 (semi-compact) and Class 4 (slender), are typically defined according to the susceptibility of the most slender element of the cross-section to local buckling, as illustrated in Fig. 1. A Class 1 cross-section is fully effective under pure compression and can develop its plastic moment capacity M_{pl} in bending with sufficient rotation capacity to allow redistribution of moments in indeterminate steel frames. A Class 2 cross-section is also fully effective in pure compression and can reach its plastic moment capacity M_{pl} but with lower (assumed to be zero in design) rotation capacity in bending. A Class 3 cross-section remains fully effective in pure compression, but in bending, local buckling now occurs after the elastic moment M_{el} but before the plastic moment M_{pl} is attained; bending resistance of a Class 3 cross-section is therefore limited to the elastic moment M_{el}, or a linearly interpolated moment between M_{el} and M_{pl} [3,4]. For a Class 4 cross-section, local buckling occurs in the elastic range prior to reaching either the yield load in compression or elastic moment in bending, and the effective width method is used to consider the effects of local buckling explicitly.

Steel design specifications [1,2] typically treat the plate elements of the cross-section individually, thus neglecting the interaction effects between adjacent elements, i.e. the ability of the less slender elements to provide some assistance in resisting local buckling to the more slender elements, and the classification of the most slender element defines that of the overall cross-section. Previous stub column tests [5,6], beam tests [7] and beam-column tests [8,9] on I-sections have shown that web-flange interaction effects can have a substantial influence on ultimate cross-section behaviour and hence the determination of its ultimate resistance. Kato [10,11] and Beg and Hladnik [12] proposed slenderness limits for Class 3 cross-sections in a form considering these web-flange interaction effects. Seif and Schafer [13] proposed analytical expressions for determining the elastic buckling stresses of hot-rolled steel I-sections considering element interaction.

Within the current cross-section classification framework, an idealised elastic, perfectly plastic material model is used, whereby the maximum stress in the cross-section is limited to the material yield stress f_y, neglecting the beneficial effects of strain hardening. In addition to highlighting the importance of element interaction effects, experimental results have also shown that this limitation often leads to conservative predictions of the resistance of stocky hot-rolled steel I-sections in both compression [14] and bending [15], due primarily to the omission of strain hardening. Furthermore, results have shown that linearly interpolating between M_{el} and M_{pl} does not offer an accurate representation of the spread of plasticity in Class 3 cross-sections [3,4].

To address these shortcomings in current codified methods, a deformation based design approach called the continuous strength method (CSM), which provides an alternative treatment to cross-section classification and enables the effective utilisation of strain hardening, has been proposed. The method was originally developed for stainless steel structural elements [16-18], which exhibit a high degree of strain hardening, and the same concept has since been applied to structural carbon steel, with a modified material model [19-21]. However, previous developments have focused on compression and bending resistances, while investigations into the cross-sectional behaviour of hot-rolled steel I-sections under combined loading have been vary limited. Hence, a comprehensive experimental and numerical simulation programme on hot-rolled steel I-sections under combined compression and bending moment has been carried out and is presented herein, with the aim of investigating the effects of the material strain hardening on the behaviour and resistance of stocky hot-rolled steel I-sections. A total of two stub column tests and 12 mono-axial or bi-axial eccentric compression tests were carried out. The experimental results were supplemented with additional data collected from the literature [3] and generated by means of validated finite element (FE) models considering different cross-section slenderness, material grades and combinations of loading. These data are then used to evaluate the current codes of practice, including EN 1993-1-1 [1] and AISC-360-16 [2], and to extend the CSM to the design of hot-rolled steel I-sections under combined loading.

2. Experimental investigation

2.1. Introduction

An experimental study comprising material testing, geometric imperfection measurements, two stub column tests, four uniaxial bending plus compression tests and 8 biaxial bending plus compression tests on hot-rolled steel I-sections was conducted at the University of Applied Sciences of Western Switzerland in order to investigate their cross-sectional behaviour and resistance under combined loading. The test specimens were categorized into two series according to their steel grade: Series ‘A’ (S235) and Series ‘B’ (S355). All the test specimens were hot-rolled HEB 160 cross-sections, which are Class 1 according to the slenderness limits of EN 1993-1-1 [1]. It was chosen to test cross-sections of compact proportions in order that material strain hardening would be experienced and hence that the influence of strain hardening on their behaviour and strength could be studied.

2.2. Material testing and initial geometric imperfection measurements

The basic stress-strain properties of the investigated hot-rolled steel I-sections were determined through 12 tensile coupon tests, with six coupons tested for each of the two steel sections (one grade S235 and the other S355). Tensile coupons were extracted from the web and flanges of the two specimens in the longitudinal (rolling) direction. Fig. 2 shows the locations from which the coupons were cut from the test specimens, together with the definition of the adopted notation, where TF and TW indicate tensile coupons cut from the flange and the web, respectively. The tensile coupons were 20 mm in width with gauge lengths of 70 mm and 90 mm for the web coupons and the flange coupons, respectively. All the tensile coupon tests were conducted in compliance with the procedures set out in EN ISO 6892-1 [22] using a 100 kN hydraulic testing machine. Once a tensile coupon had been gripped, a 20 mm clip gauge was affixed to the mid-height of the coupons to measure the longitudinal strain and elongation. A constant rate of strain (0.045%/s) was applied until fracture.

Typical measured stress-strain curves from the flange and the web tensile coupons from the two cross-sections are shown in Fig. 3. All the tensile coupons exhibited the anticipated sharply defined yield point, followed by a yield plateau before the initiation of strain hardening. The material properties obtained from all tensile coupon tests are summarized in Table 1, including the modulus of elasticity E, the yield stress f_y, the ultimate tensile stress f_u, the yield-to-ultimate tensile stress ratio f_y/f_u, the strain hardening strain ε_{sh} (where the yielding plateau ends and subsequently the strain hardening initiates) and the strain at the ultimate tensile stress ε_u. The material properties of hot-rolled steel cross-sections are generally fairly homogeneous, although higher yield strengths are often observed in thinner material due to the more rapid cooling. This trend is seen in the present study, where the yield strength of the thinner web is higher than that of the flanges (see Table 1).

Initial local geometric imperfections were measured for all the specimens prior to testing. Since all the specimens presented in this paper are short columns that are not susceptible to global buckling, only local imperfections were considered. The measurements were conducted by means of an aluminium perforated bar holding 7 equally-spaced displacement transducers (LVDTs) which was moved laterally across the flat faces of each specimen (see Fig. 4) in order to develop 3D geometrical representation of the sections, a typical example of which is shown in Fig. 5. Note that the measurements of the 7 LVDTs were started and finished 50 mm away from the ends of the specimens in order to eliminate the possible influence of welding on the local imperfection measurements. The measured maximum local geometric imperfection amplitudes from the flange faces (ω_f) and the web face (ω_w) of the specimens are reported in Tables 2 and 3.

2.3. Stub column tests

For each of the two test series (grades S235 and S355 steel), one concentrically-loaded stub column test was performed in order to determine the cross-sectional load carrying capacity under pure compression as well as to assess the influence of material strain hardening on the cross-sectional resistance. The nominal length for each specimen was chosen to be approximately three times the height of the cross-section, to be short enough to avoid global flexural buckling, but sufficiently long to contain representative local geometric imperfection and residual stress patterns [23]. The ends of the columns were milled flat and perpendicular to the longitudinal axis of the column, and endplates with a thickness of 30 mm were welded to the ends of the specimens to ensure a uniform distribution of load during testing and to avoid premature end failures. The testing machine was a 3000 kN capacity hydraulic rig and the stub columns were loaded under displacement control up to and beyond their peak loads, with the rate of displacement kept constant at 0.025 mm/s until the peak load, and the rate increased soon after. The testing setup for the stub columns is shown in Fig. 6. Four LVDTs were employed at each end to determine the average end shortening of the specimens and three strain gauges, mounted to the column mid-faces at mid-height, were used to measure the longitudinal strains. An additional LVDT was used at mid-height between the flanges to detect the initiation of local buckling, if any, as shown in Fig. 6.

Table 2 presents the measured cross-section dimensions for the specimens tested under pure compression using the nomenclature from Fig. 2, where L is the length of the specimen, B and

H are the outer width and depth of the cross-section, respectively, t_f is the flange thickness, t_w is the web thickness, r_i is the internal corner radius and A is the cross-sectional area.

The strain gauge readings provided a more accurate means of determining the initial axial stiffness of the stub columns than the LVDTs, since the LVDT measurements include not only the end shortening of the specimen but also the elastic deformation of the endplates. Thus, a correction that combines both sets of measurements was required to get the true end shortening values, following the method recommended in [24]. Table 2 also summarizes the corrected test results of the stub columns, including the ultimate axial load N_u, the corresponding true end shortening at the ultimate load δ_u and ultimate load normalised by the squash load $N_u/Af_{y,wa}$, where $f_{y,wa}$ is the weighted average material yield stress based on the tensile coupon test results given in Table 1 for the flanges and web and their respective areas. The stub column specimens generally failed by inelastic local buckling at mid-height, as shown for specimen B7 in Fig. 7. The full load-end shortening curves for the stub columns are presented in Fig. 8, while the normalized load-end shortening curves are depicted in Fig. 9, where N_y is the yield load $N_y = Af_{y,wa}$, highlighting the more prominent role of strain hardening for the S235 specimen (Specimen A7) than the S355 specimen (Specimen B7).

2.4. Combined loading tests

In the combined loading tests, uniaxial and biaxial bending plus compression was achieved through the application of eccentric compression. For each of the two series, two uniaxial bending plus compression tests - one bending about the major axis and the other bending about the minor axis, and four biaxial bending plus compression tests were carried out to investigate the cross-sectional behaviour of hot-rolled steel I-sections under combined loading. The measured cross-section dimensions and maximum local imperfection amplitudes of the specimens are presented in Table 3, following the nomenclature from Fig. 1.

As shown in Fig. 10, the loading rig consisted of a hydraulic actuator at the lower end of the specimen and a fixed top platten. Two hemispherical bearings were specially designed to provide pinned-pinned end restraints for the test specimens. Endplates were welded to the specimens at different eccentricities to generate a range of bending moment to axial loading ratios, and then bolted to the hemispherical bearings of the 3000 kN test machine. Each of the two bearings contained two T-shaped grooves, which enabled adjustment of the specimens when bolted to the endplates to achieve loading at the specified eccentricities. The bolts were pre-tensioned in order to prevent uplift or detachment of the specimen endplates from the hemispherical bearings.

Tests were carried out under displacement control in order to capture the post-ultimate behaviour of the specimens, at a rate of 0.025 mm/s. During testing, eight LVDTs placed at both ends of the test specimens were used to measure axial shortening and end rotation. In addition, two further LVDTs were used at the mid-height of the specimens in order to measure the lateral deflections in both principal directions, allowing the generated second order bending moments to be calculated. Two inclinometers, placed at each end of the test specimens, were used for measuring end rotations. Four strain gauges, two attached to the mid-face of each flange and the other two attached to the extreme fibres of one flange at mid-height of the specimen, were used to measure the longitudinal strains and to determine the calculated loading eccentricities. The applied load and readings from the LVDTs, inclinometers and strain gauges were recorded using a data logger at half-second intervals (2 Hz) during the tests.

The measurements from the strain gauges can be used to determine the calculated loading eccentricities e_0, to enable an accurate evaluation of the tests and FE results, as well as a fair assessment of the design methods. For each axis of bending, the flexural strain ε_m due to the bending moment can be derived through Eq. (1):

$$\varepsilon_\mathrm{m} = \frac{\varepsilon_\mathrm{max} - \varepsilon_\mathrm{min}}{2} \tag{1}$$

where ε_max is the measured strain at the maximum compressive fibre and ε_min is the measured maximum tensile or minimum compressive strain at the other extreme fibre. The total bending moment M_T, considering both the first order bending moment M_1 due to the eccentricity of the applied force N and the second order bending moment M_2 due to the lateral deflection at mid-height $\mathit{\Delta}$, can be calculated as:

$$M_\mathrm{T} = M_1 + M_2 = Ne_0 + N\mathit{\Delta} \tag{2}$$

The total bending moment can also be expressed, in the elastic range, as $M_\mathrm{T} = EI\kappa$, where E is the Young's modulus, I is the second moment of area about the axis of bending and κ is the curvature which can be determined, assuming plane sections remain plane and normal to the neutral axis during bending, from the readings of the strain gauges. The curvature is given by $\kappa = \varepsilon_\mathrm{m} / 0.5d$, where d is the distance between the extreme fibres in the corresponding bending axis. Therefore, the calculated loading eccentricity e_0 can be determined from Eq. (3). Note that since Eq. (3) is only applicable in the elastic range, the average value of the eccentricities, obtained during the early stage of loading, was taken as the calculated loading eccentricity e_0 for each test. Overall, the calculated loading eccentricities e_0 were found to be in reasonably good agreement with the measured loading eccentricities e_m, as shown in Table 4, but e_0 is considered to be more accurate than e_m and is therefore used in the following analyses.

$$e_0 = \frac{EI(\varepsilon_{\max} - \varepsilon_{\min})}{dN} - \mathit{\Delta} \tag{3}$$

Table 4 summarizes the key results from the specimens tested under combined loading, including the ultimate load N_u, the end rotation at the ultimate load θ_u, the measured loading eccentricity e_m, the calculated loading eccentricity e_0, the mid-height lateral deflection at ultimate load $\mathit{\Delta}_u$ and the total bending moment at ultimate load $M_{T,u}$, where the suffixes ‘y’ and ‘z’ denote bending about the major axis and the minor axis, respectively.

The specimens generally failed by material yielding, though inelastic local buckling was also observed for some test specimens at large deformations. Representative failure modes for the uniaxial and biaxial bending plus compression tests are illustrated in Fig. 11(a) and (b), respectively. The full experimental load-end rotation curves for each specimen subjected to uniaxial or biaxial bending plus compression loading are presented in Fig. 12(a)-(f). The influence of material strain hardening on the cross-sectional resistance is carefully explored in the companion paper [25].

3. Finite element modelling

Following the experimental investigation, a numerical study of hot-rolled steel I-sections under combined loading, using the nonlinear FE analysis programme ABAQUS [26], was carried out, and is described in this section. The aims of the numerical study were to capture the physical behaviour observed in the experiments and to investigate the cross-sectional resistance of hot-rolled steel I-sections under combined loading. The FE models were firstly validated against the test results and subsequently used to perform parametric studies, described in the companion paper [25], to generate additional data over a wide range of cross-section slenderness and loading combinations.

3.1. Finite element model

In order to represent accurately the behaviour of the test specimens, suitable FE models need to be developed. The four-noded doubly curved shell element S4R with reduced integration was selected for the modelling of the test specimens in this investigation, which has been shown in the literature to be suitable for similar problems [3,27,28]. The endplates were modelled using the same shell elements S4R with an equivalent thickness of 30 mm and modelled with elastic material behaviour since the endplates remained elastic during loading. The finite element model was meshed using 20 elements along the flange width, 20 elements along the web height, with a finer mesh of 2 elements in each fillet zone of the cross-section, and 100 elements along the length of the specimen. The selected mesh size gave a sufficient degree of accuracy with acceptable computational cost.

Particular attention was given to ensure that the properties of the fillet zones, as shown in Fig. 13, could be accurately represented. The nodes at each end of the web were shifted by a distance of half the flange thickness to avoid overlapping of the elements at the web-to-flange junction, and these nodes were tied to their corresponding nodes at the mid-thickness of the flanges using “General multi-point constraints (*MPC)”, which ensured that both the translational and rotational degrees of freedom were equal for this pair of nodes. The additional area and moments of inertia due to the fillet zones were allowed for by increasing the thickness of the adjacent web elements (see Fig. 13).

The average material stress-strain responses from the flanges and web, represented by the bilinear plus non-linear hardening model proposed by Yun and Gardner [19], were employed in the FE models for the validation study. The engineering stress-strain curve was converted into the format of true stress and logarithmic plastic strain, as required in ABAQUS [26] for the element type adopted, according to Eqs. (4) and (5), in which σ_{nom} is the engineering stress, $\varepsilon_{\mathrm{nom}}$ is the engineering strain and σ_{true} and $\varepsilon_{\mathrm{ln}}^{\mathrm{pl}}$ are the true stress and logarithmic plastic strain, respectively.

$$\sigma_{\mathrm{true}} = \sigma_{\mathrm{nom}}(1+\varepsilon_{\mathrm{nom}}) \tag{4}$$

$$\varepsilon_{\mathrm{ln}}^{\mathrm{pl}} = \ln(1+\varepsilon_{\mathrm{nom}}) - \frac{\sigma_{\mathrm{true}}}{E} \tag{5}$$

The interfaces between the endplates and the specimen were modelled using a constraint pair, where the endplates were the master surfaces and the end cross-sections of the specimen were the slave surfaces. This constraint provides a simple means of bonding surfaces together in terms of all the translational and rotational degrees of freedom. Each endplate was then coupled to a reference point located at an eccentricity corresponding to the calculated loading eccentricity e_0. Note that the reference point was also offset longitudinally from the end cross-section of the specimens by 172 mm (equal to the distance from the end cross-section to the centroid of the hinge) for the combined loading tests, in order to accurately model the effective length of the specimens L_e, as shown in Fig. 10. The axial compressive force was applied at the bottom reference point following the test procedure. For the stub column FE models, which were under pure axial compression, the concentric reference points were restrained against all degrees of freedom, only allowing longitudinal translation at the bottom reference point. For the combined loading FE models, all degrees of freedom were restrained at the reference points except for longitudinal translation at the bottom reference point and rotation about the axis of bending for both reference points, to simulate pin-ended boundary conditions.

Initial local geometric imperfections were incorporated into the FE models in the form of the lowest elastic buckling mode shape arising under axial compression; this results in a perturbed mesh throughout the cross-section and provides comparable local imperfections for all specimens. It has been found that the sensitivity of the numerical results to the initial geometric imperfections, both the shapes and amplitudes, is relatively low for non-slender hot-rolled steel I-sections [29]. The imperfection amplitude was taken as $a/200$ (a being the flat width of the most slender constituent plate element in the cross-section under compression), which approximately represented the average maximum web imperfection amplitudes measured in the test specimens and is also in accordance with the recommendations in [29,30], for all the FE simulations in this study.

The residual stress patterns recommended by the European Convention for Constructional Steelwork (ECCS) [31], as shown in Fig. 14, where compressive residual stresses are designated as positive and tensile residual stresses as negative, were applied to the FE models. The magnitude of the residual stress depends on whether the height to width ratio of the cross-section is less than or equal to 1.2 or greater than 1.2 and is independent of the yield stress, with the nominal stress f_y^*=235 MPa taken as the reference value. The modified Riks method was used as the solution scheme for the FE simulations to allow the post-ultimate path of the modelled specimens to be captured.

3.2. Validation of the FE models

Validation of the FE models was based on the comparison of the numerically obtained results with the relevant data from the conducted tests. The ultimate load $N_{\mathrm{u,test}}$, the end rotations at ultimate load $\theta_{\mathrm{u,test}}$, and the mid-height lateral deflection at ultimate load $\Delta_{\mathrm{u,test}}$ obtained from the tests were compared with the corresponding numerical values $N_{\mathrm{u,FE,}}$ $\theta_{\mathrm{u,FE}}$ and $\Delta_{\mathrm{u,FE}}$ predicted by the FE models, as reported in Table 5. Overall, good agreement between experimental and numerical results can be seen, particularly in terms of the ultimate load N_{u}, with the mean value of the ratio of $N_{\mathrm{u,FE}}/N_{\mathrm{u,test}}$ being 0.96 and the COV being 0.03. The end rotations θ_{u} and mid-height lateral deflection at ultimate load Δ_{u} less accurately captured, but acceptably predicted, and although in some cases the numerical values deviated from the corresponding test values by more than 30%, the absolute differences were relatively small. Good agreement between the failure modes of the tested and simulated specimens was also obtained, typical examples of which are shown in Fig. 11 (Specimens B3 and B5).

Figs 15 and 16 show comparisons between the numerical load-deformation curves and the corresponding experimental curves from the stub column tests and bending plus compression tests, respectively. The load-deformation curves obtained from the FE models but without considering the effect of material strain hardening (i.e. using an elastic-perfectly plastic material model) have also been plotted in Figs 15 and 16 for comparison. It can be seen from Figs 15 and 16 that the material strain hardening has a significant influence on the post-ultimate behaviour of all specimens and on the ultimate capacity of some. In general, the curves obtained from the FE models with strain hardening tend to show a more gradual loss of strength in the post-ultimate region, while the curves without considering the effect of strain hardening tend to have a more accentuated post-peak drop in strength. There is also consistently a more significant influence of strain hardening (on both ultimate and post-ultimate behaviour) for the hot-rolled I-sections under compression and major axis bending plus compression then for the other loading scenarios; this is because, for a given level of outer-fibre strain, a greater proportion of the cross-sectional area enters the strain hardening regime in the former cases. Overall, it can be seen that accurate replication of the initial stiffness, ultimate load and general form of the load-deformation histories was achieved by the developed FE models. The small differences in initial stiffness between the numerical and experimental results are attributed to contributions from non-explicitly modelled sources, such as small levels of friction in the hinges, out-of-flatness of the endplates and unexpected eccentricities, while the generally slightly conservative FE predictions of ultimate strength (more notably for the specimens in compression and compression plus major axis bending) may be due to variation in material stress-strain properties around the cross-sections, which is not fully captured by the results of the tensile coupon tests that are performed on material extracted at discrete locations from within the cross-sections [32,33]. In particular, stress-strain curves obtained from tensile tests on full structural sections were found to have consistently shorter yield plateaus (and hence earlier initiation of strain hardening) then those obtained from coupon tests [32,33].

The accuracy of the FE models has been further verified by comparing the numerically obtained ultimate load $N_{\mathrm{u,FE}}$ with the respective test values from compression tests of 22 semi-compact I-sections [3]. The comparisons between the test and FE results are presented in Table 6 for both stub columns and combined loading tests, where the definitions of the loading eccentricity e and angle α are shown in Fig. 17. The FE models show excellent ability to predict the ultimate resistances of hot-rolled steel semi-compact I-sections, with the mean numerical-to-test ratio $N_{\mathrm{u,FE}}/N_{\mathrm{u,test}}$ very close to unity and with small scatter. The comparisons between the test results and numerical predictions have led to the conclusion that the developed FE models are accurate and reliable for predicting the ultimate resistances of hot-rolled steel I-sections subjected to combined loading and, thus, suitable for performing the comprehensive parametric studies presented in the companion paper.

4. Conclusions

A total of 14 experiments on hot-rolled steel I-sections, consisting of two different material grades, subjected to either compression or combined loading has been carried out and presented in this paper. The test specimens were stocky (compacted) cross-sections and all were Class 1 according to EN 1993-1-1 [1]. The stockiness of the tested cross-sections was such that material strain hardening had an influence on their cross-sectional capacity and this influence is assessed in the companion paper. Parallel numerical analysis of hot-rolled steel I-sections under different loading conditions was performed using the finite element (FE) modelling program ABAQUS. The FE models were validated against the test results obtained in the present paper and from the literature [3]. It was found that the FE models were capable of replicating accurately the structural behaviour of the test specimens, and are therefore suitable for performing parametric studies, as presented in the companion paper. The combined experimental and numerical results, which cover a range of cross-section slenderness, material grades and combinations of loading, are then used to assess the accuracy of the current codified design provisions for hot-rolled steel I-sections under combined loading and to extend the scope of application of a more efficient deformation based design approach, the continuous strength method (CSM), to such cases.

Acknowledgements

The authors would like to thank Mr. Yanis Schaller, Mr. Jean-Paul Andrey and Mr. Dominique Delaquis for their assistance in the experimental programme. The financial support provided by the China Scholarship Council (CSC) for the first author’s PhD study at Imperial College London is gratefully acknowledged.

Notation

The following symbols are used in this paper:

A = cross-section area;

a = flat width of the most slender constituent plate element in the cross-section under compression;

B = width of section;

d = distance between the extreme fibres;

E = Young’s modulus;

e = distance between loading point and centroid of cross-section;

e_{m} = measured loading eccentricity;

e_0 = calculated loading eccentricity;

f_{y} = yield stress;

$f_{\mathrm{y,aw}}$ = weighted average material yield stress;

f_{u} = ultimate tensile stress;

H = depth of section;

I = second moment of area;

L = length of specimen;

L_{e} = effective length of specimen;

M_{el} = elastic moment capacity;

M_{pl} = plastic moment capacity;

M_{T} = total bending moment;

$M_{\mathrm{T,u}}$ = total bending moment at ultimate load;

$M_1 = Ne_0$ is the first order bending moment;

$M_2 = N\varDelta$ is the second order bending moment;

N = axial load;

N_u = ultimate axial load;

$N_y = Af_{y,aw}$ is the yield load;

r_i = web-flange internal corner radius;

t_f = flange thickness;

t_w = web thickness;

α = angle to define the position of eccentric loading;

ε_{ln}^{pl} = logarithmic plastic strain;

ε_m = flexural strain due to bending moment;

ε_{max} = measured strain at the maximum compressive fibre;

ε_{min} = measured maximum tensile or minimum compressive strain at the other extreme fibre;

ε_{nom} = engineering strain;

ε_{sh} = strain hardening strain;

ε_u = strain at ultimate tensile stress;

$\varepsilon_y = f_y/E$ is the yield strain;

σ_{nom} = engineering stress;

σ_{true} = true stress;

δ_u = end shortening of stub columns at ultimate load;

κ = curvature under bending moment;

θ = end rotation;

θ_u = end rotation at ultimate load;

ω_f = measured maximum local geometric imperfection amplitudes from the flange faces of test specimens;

ω_w = measured maximum local geometric imperfection amplitudes from the web face of test specimens;

Δ = lateral deflection at mid-height of specimens;

Δ_u = mid-height lateral deflection at ultimate load;

Suffixes ‘y’ and ‘z’ denote bending about the major and the minor axis, respectively, and Suffixes ‘test’ and ‘FE’ denote results obtained from experiments and FE models, respectively.

References

[1] EN 1993-1-1. Eurocode 3: Design of steel structures – Part 1-1: General rules and rules for buildings. Brussels: European Committee for Standardization (CEN); 2005.

[2] ANSI/AISC 360-16. Specification for structural steel buildings. Chicago, Illinois: American Institute of Steel Construction (AISC); 2016.

[3] Kettler M. Elastic-plastic cross-sectional resistance of semi-compact H-and hollow sections. PhD thesis, Faculty of Civil Engineering, Graz University of Technology, Graz, Austria; 2008.

[4] Boissonnade N, Jaspart JP, Oerder R, Weynand K. A new design model for the resistance of steel semi-compact cross-sections. Proc., 5th European Conf. on Steel Structures, Eurosteel, Graz, Austria; 2008.

[5] Davids AJ, Hancock GJ. Compression tests of short welded I-sections. J Struct Eng (ASCE) 1986;112(5):960-76.

[6] Ren WX, Zeng QY. Interactive buckling behaviour and ultimate load of I-section steel columns. J Struct Eng (ASCE) 1997;123(9):1210-17.

[7] Bradford MA. Inelastic local buckling of fabricated I-beams. J Constr Steel Res 1987;7(5):317-34.

[8] Hasham AS, Rasmussen KJR. Section capacity of thin-walled I-section beam-columns. J Struct Eng (ASCE) 1998;124(4):351-59.

[9] Hasham AS, Rasmussen KJR. Interaction curves for locally buckled I-section beam-columns. J Constr Steel Res 2002;58(2):213-41.

[10] Kato B. Rotation capacity of H-section members as determined by local buckling. J Constr Steel Res 1989;13(2):95-109.

[11] Kato B. Deformation capacity of steel structures. J Constr Steel Res 1990;17(1):33-94.

[12] Beg D, Hladnik L. Slenderness limit of class 3 I cross-sections made of high strength steel. J Constr Steel Res 1996;38(3):201-17.

[13] Seif M, Schafer BW. Local buckling of structural steel shapes. J Constr Steel Res 2010;66(10):1232-47.

[14] Foster A. Stability and design of steel beams in the strain-hardening range. Ph.D. thesis, Department of Civil and Environmental Engineering, Imperial College London, London, U.K; 2014.

[15] Byfield MP, Nethercot DA. An analysis of the true bending strength of steel beams. Proc Inst Civ Eng Struct Build 1998;128(2):188-97.

[16] Gardner L, Nethercot DA. Stainless steel structural design: A new approach. Struct Eng 2004;82(21):21-28.

[17] Afshan S, Gardner L. Experimental study of cold-formed ferritic stainless steel hollow sections. J Struct Eng (ASCE) 2013;139(5):717-28.

[18] Ashraf M, Gardner L, Nethercot DA. Structural stainless steel design: Resistance based on deformation capacity. J Struct Eng (ASCE) 2008;134(3):402-11.

[19] Yun X, Gardner L. Stress-strain curves for hot-rolled steels. J Constr Steel Res 2017;133: 36-46.

[20] Yun X, Gardner L, Boissonnade N. The continuous strength method for the design of hot-rolled steel cross-sections. Eng Struct 2018; 157:179-191.

[21] Gardner L,Yun X, Macorini L, Kucukler M. Hot-rolled steel and steel-concrete composite design incorporating strain hardening. Structures 2017;9:21-28.

[22] ISO 6892-1. Metallic materials – Tensile testing Part 1: Method of test at ambient temperature. Brussels: European Committee for Standardization (CEN); 2009.

[23] Ziemian RD. Guide to stability design criteria for metal structures, 6th Ed., Wiley, Hoboken, NJ; 2010.

[24] Compression tests of stainless steel tubular columns. Tech Rep S770, Centre for Advanced Structural Engineering. University of Sydney, Australia; 1990.

[25] Yun X, Gardner L, Boissonnade N. Ultimate capacity of I-sections under combined loading – Part 2: Parametric studies and CSM design. J Constr Steel Res 2018; (submitted).

[26] ABAQUS Version 6.13. Hibbit, Karlsson and Sorensen, Pawtucket, RI.

[27] Ashraf M, Gardner L, Nethercot DA. Finite element modelling of structural stainless steel cross-sections. Thin-Walled Struct 2006;44(10):1048-62.

[28] Becque J, Rasmussen KJR. Numerical investigation of the interaction of local and overall buckling of stainless steel I-columns. J Struct Eng (ASCE) 2009;135(11):1349-56.

[29] Yun X, Nseir J, Gardner L, Boissonnade N. Experimental and numerical investigation into the local imperfection sensitivity of hot-rolled steel I-sections. Proc., 7th Int. Conf. on Coupled Instabilities in Metal Structures, Baltimore, Maryland, U.S.; 2016.

[30] EN 1993-1-5. Eurocode 3: Design of steel structures – Part 1-5: Plated structural elements. Brussels: European Committee for Standardization (CEN); 2006.

[31] Ultimate limit state calculation of sway framed with rigid joints. Technical Committee 8 of European Convention for Constructional Steelwork (ECCS), Tech. Rep., No. 33; 1984.

[32] Wang J, Afshan S, Schillo N, Theofanous M, Feldmann M, Gardner L. Material properties and compressive local buckling response of high strength steel square and rectangular hollow sections. Eng Struct 2017;130:297-315.

[33] Foster ASJ, Gardner L, Wang Y. Practical strain-hardening material properties for use in deformation-based structural steel design. Thin-Walled Struct 2015;92:115-129.

Tables:

Table 1. Measured material properties from tensile coupon tests

Label	E (N/mm^2)	f_y (N/mm^2)	f_u (N/mm^2)	ε_{sh} (%)	ε_u (%)	f_u/f_y
S235 TF1	-	322	464	1.62	17.99	1.44
S235 TF2	193500	303	455	1.27	18.83	1.50
S235 TF3	198800	300	453	1.44	19.64	1.51
S235 TF4	195800	316	457	1.33	17.79	1.45
S235 TW1	-	365	494	1.75	14.66	1.35
S235 TW1	192800	386	488	1.92	15.01	1.26
S355 TF1	210200	393	518	2.03	13.23	1.32
S355 TF2	205100	392	494	2.55	13.56	1.26
S355 TF3	208600	386	507	2.14	12.94	1.31
S355 TF4	213000	388	504	2.17	13.56	1.30
S355 TW1	202400	405	520	2.00	11.80	1.29
S355 TW1	199500	405	519	1.79	12.74	1.28

Table 2. Measured geometrical parameters and key test results of stub column specimens

Specimen ID	L (mm)	B (mm)	H (mm)	t_f (mm)	t_w (mm)	r_i (mm)	A (mm^2)	ω_f (mm)	ω_w (mm)	N_u (kN)	δ_u (mm)	$N_\mathrm{u}/Af_{\mathrm{y,wa}}$
A7	500	161.44	160.80	13.00	8.61	15.00	5552	0.47	0.34	2316.3	12.27	1.25
B7	500	160.80	161.15	12.20	8.20	15.00	5238	2.65	0.89	2420.0	15.31	1.16

Table 3. Measured geometrical parameters of specimens under combined loading

Specimen ID	Axis of bending	L (mm)	B (mm)	H (mm)	t_f (mm)	t_w (mm)	r_i (mm)	ω_f (mm)	ω_w (mm)
A2	Major axis	500	161.16	161.06	13.06	8.58	15.00	0.20	0.20
B2		500	160.65	161.30	12.00	8.00	15.00	0.68	0.34
A5	Minor axis	500	161.40	161.02	12.99	8.57	15.00	0.36	0.21
B5		500	160.80	161.15	12.20	8.30	15.00	2.51	0.75
A1	Bi-axial	500	160.96	161.19	13.07	8.60	15.00	0.26	0.26
A3		500	161.41	161.05	12.99	8.66	15.00	0.35	0.68
A4		500	161.08	161.23	12.99	8.48	15.00	1.46	0.44
A6		500	161.68	161.01	12.94	8.50	15.00	0.19	0.14
B1		500	160.80	161.20	12.15	8.20	15.00	1.12	1.04
B3		500	160.80	161.15	12.20	8.20	15.00	1.80	0.29
B4		500	160.95	160.90	12.25	8.30	15.00	0.66	0.76
B6		500	160.80	161.15	12.15	8.20	15.00	4.15	0.19

Table 4. Summary of key test results of specimens under combined loading

Specimen ID	Axis of bending	N_{u} (kN)	$e_{m,y}$ (mm)	$e_{0,y}$ (mm)	$e_{m,z}$ (mm)	$e_{0,z}$ (mm)	$\Delta_{u,y}$ (mm)	$\Delta_{u,z}$ (mm)	$\theta_{u,y}$ (deg)	$\theta_{u,z}$ (deg)	$M_{T,u,y}$ (kNm)	$M_{T,u,z}$ (kNm)
A2	Major axis	1157.7	75.0	70.2	-	-	15.70	-	4.90	-	99.5	-
B2		1183.3	75.0	75.1	-	-	21.00	-	3.72	-	113.7	-
A5	Minor axis	943.6	-	-	45.0	44.8	-	6.90	-	1.53	-	48.8
B5		1138.8	-	-	45.0	44.6	-	6.40	-	1.40	-	64.9
A1	Bi-axial	1302.8	30.0	28.8	20.0	21.8	1.59	2.90	0.34	0.77	39.5	32.2
A3		1191.6	15.0	15.0	30.0	27.8	0.99	6.49	0.16	1.33	19.1	40.9
A4		879.2	75.0	75.1	30.0	29.8	2.97	3.66	0.60	0.78	68.6	29.4
A6		827.2	45.0	46.0	50.0	50.6	1.74	9.10	0.38	1.36	39.5	49.4
B1		1514.5	30.0	30.1	20.0	19.7	3.14	5.40	0.42	0.73	50.3	38.0
B3		1359.6	15.0	17.7	30.0	27.7	1.26	7.69	0.18	1.10	25.8	48.2
B4		993.5	75.0	75.5	30.0	31.2	3.19	5.48	0.67	0.88	78.2	36.5
B6		952.6	45.0	45.4	50.0	50.6	2.08	7.07	0.40	1.13	45.3	54.9

Table 5. Comparison of the experimental and numerical results for hot-rolled I-sections under different loading conditions

Specimen ID	Loading condition	$N_{u,FE}/N_{u,test}$	$\theta_{u,y,FE}/\theta_{u,y,test}$	$\theta_{u,z,FE}/\theta_{u,z,test}$	$\Delta_{u,y,FE}/\Delta_{u,y,test}$	$\Delta_{u,z,FE}/\Delta_{u,z,test}$
A7	Pure compression	0.90	-	-	-	-
B7		0.92	-	-	-	-
A2	Major aixs bending plus compression	0.93	0.72	-	0.53	-
B2		0.95	0.78	-	1.06	-
A5	Minor aixs bending plus compression	1.00	-	0.89	-	0.84
B5		0.96	-	0.82	-	0.92
A1	Biaxial bending plus compression	0.93	0.65	1.06	1.06	1.60
A3		0.98	1.28	0.79	0.90	0.77
A4		0.96	0.77	0.45	1.01	1.25
A6		0.96	0.82	0.79	1.02	0.71
B1		0.95	0.96	1.57	0.54	0.94
B3		1.01	1.03	1.02	0.94	0.63
B4		0.98	0.78	0.85	1.42	1.27
B6		0.97	0.85	1.01	0.87	0.91
Mean		0.96	0.86	0.92	0.93	0.98
COV		0.03	0.21	0.30	0.28	0.31

Table 6. Comparison between numerical and experimental results for the Class 3 (semi-compact) I-sections

Section and Material	Specimen	L (mm)	Loading conditions	Eccentricity e (mm)	Angle α (deg)	$N_{\mathrm{u,test}}$ (kN)	$N_{\mathrm{u,FE}}$ (kN)	$N_{\mathrm{u,FE}}/N_{\mathrm{u,test}}$
HE 260 AA S235	sc_A1-2	900	Major axis bending plus compression	303.6	-0.3	585.2	544.1	0.93
	sc_A1-3			301.7	0.3	812.4	798.4	0.98
	sc_A2-1		Biaxial bending plus compression	301.8	9.5	556.9	545.1	0.98
	sc_A2-2			298.1	11.0	554.3	543.3	0.98
	sc_A3-1			299.9	40.9	404.5	398.7	0.99
	sc_A3-2			298.2	39.6	396.6	405.8	1.02
	sc_A4-1		Minor axis bending plus compression	98.9	90.1	826.8	857.0	1.04
	sc_A4-2			97.8	90.4	824.8	865.2	1.05
	sc_A10-2			95.8	89.6	853.4	879.9	1.03
	sc_A5-1		Axial compression	0.0	0.0	2135.0	2068.3	0.97
	sc_A5-2			0.0	0.0	2134.0	2068.3	0.97
HE 260 AA S355	sc_A7-1	900	Major axis bending plus compression	299.2	-0.2	809.6	836.0	1.03
	sc_A7-2			298.5	-0.3	772.3	837.5	1.08
	sc_A1-1			300.2	-0.1	768.5	833.9	1.08
	sc_A8-1		Biaxial bending plus compression	298.8	10.5	790.7	800.7	1.01
	sc_A8-2			298.6	11.4	769.9	794.7	1.03
	sc_A9-1			299.4	39.7	559.1	608.4	1.09
	sc_A9-2			299.1	39.8	602.4	608.4	1.01
	sc_A10-1		Minor axis bending plus compression	99.3	89.7	1299.7	1288.8	0.99
	sc_A10-3			99.4	90.1	1408.6	1361.4	0.97
	sc_A11-1		Axial compression	0.0	0.0	3138.4	3164.2	1.00
	sc_A11-2			0.0	0.0	3252.3	3164.2	0.97
							Mean	1.01
							COV	0.04

Figures:

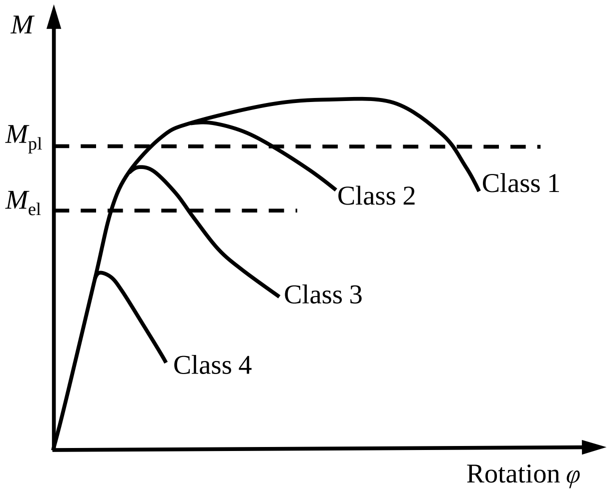

Fig. 1. Typical response and cross-section classification of steel sections in bending

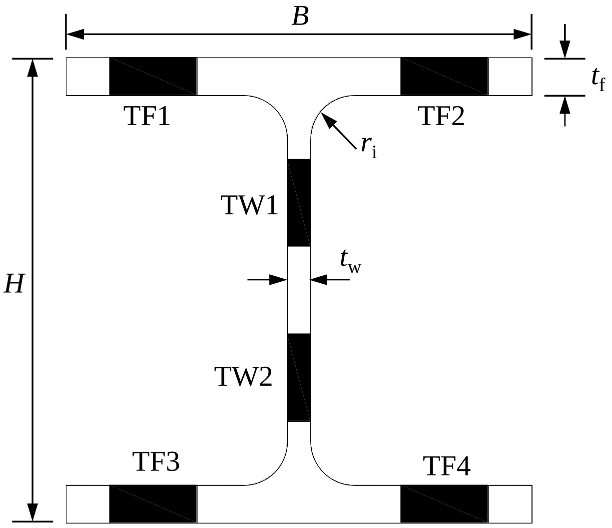

Fig. 2. Definition of symbols and location of tensile coupons in tested cross-sections

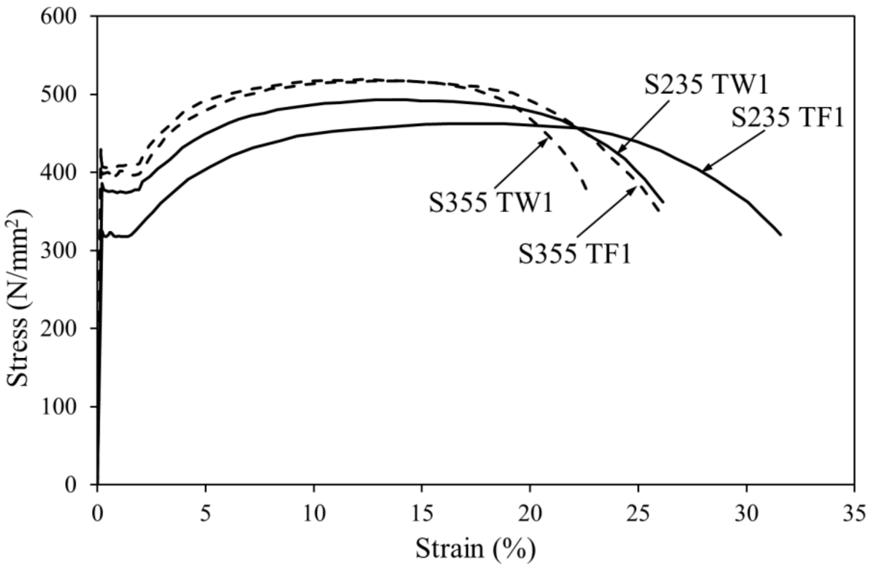

Fig. 3. Typical measured stress-strain curves from S235 and S355 specimens

Fig. 4. Test setup for geometric imperfection measurements

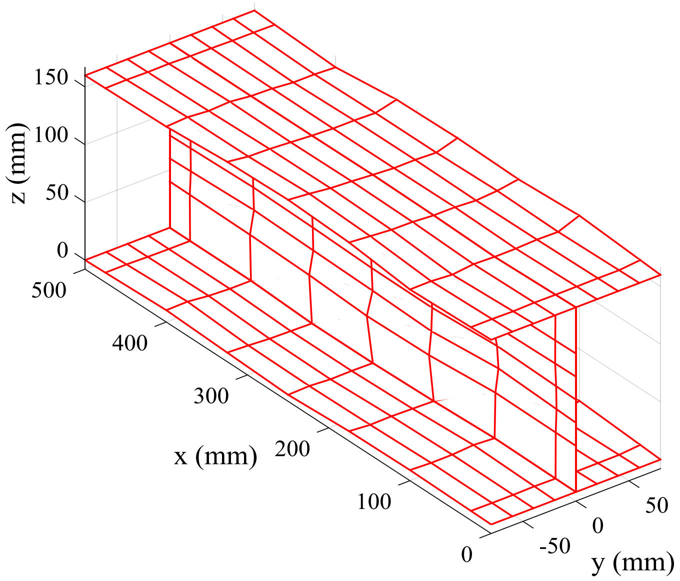

Fig. 5. Typical measured initial local geometric imperfection profile (×40)

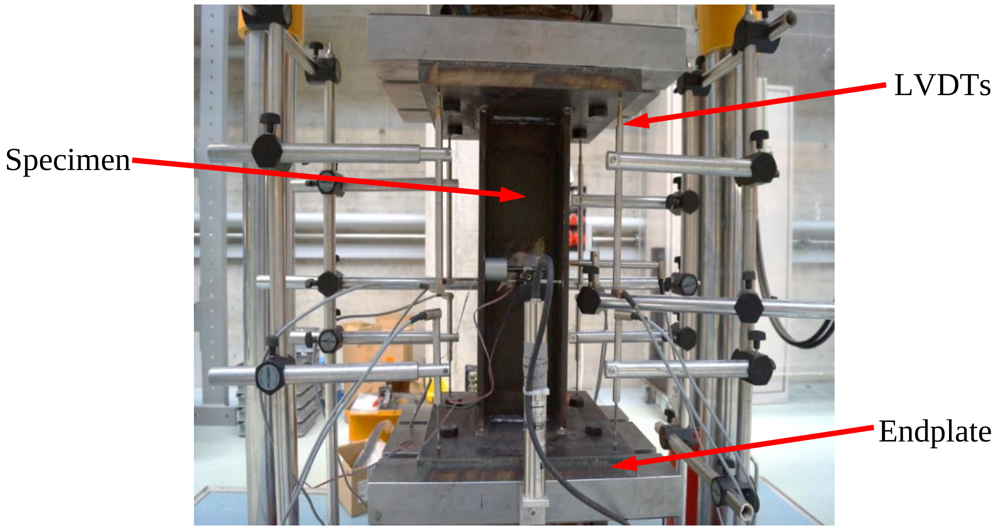

Fig. 6. Testing setup for stub columns

Fig. 7. Typical failure mode of stub columns (B7)

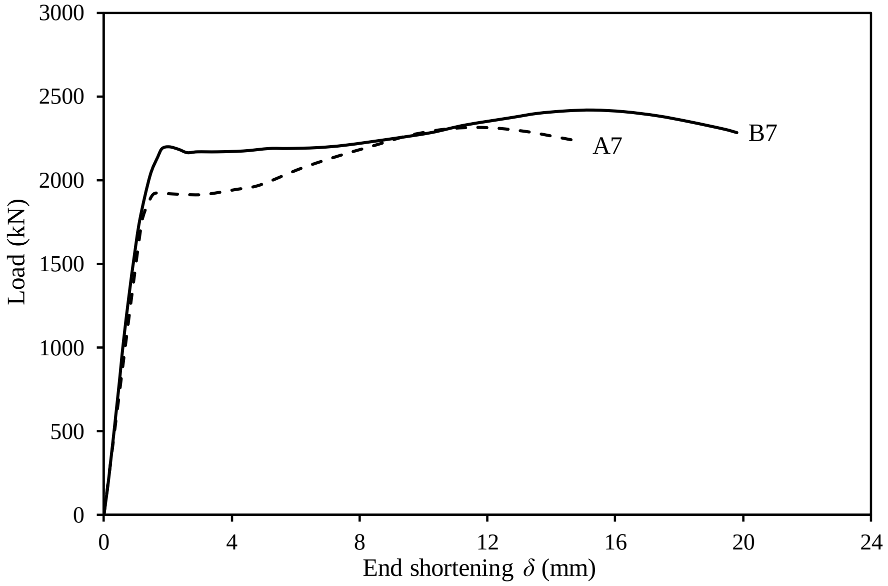

Fig. 8. Load-end shortening curves for stub column specimens

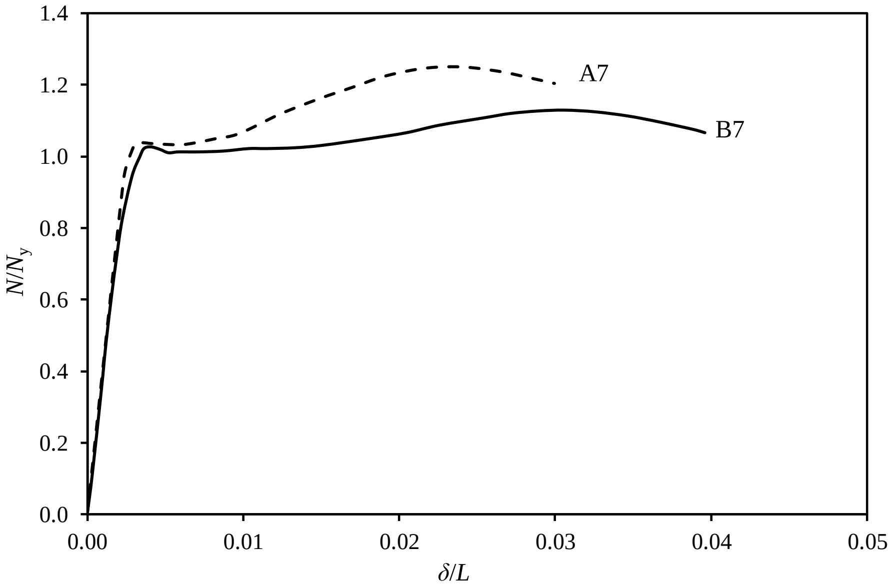

Fig. 9. Normalized load-end shortening response for stub column specimens

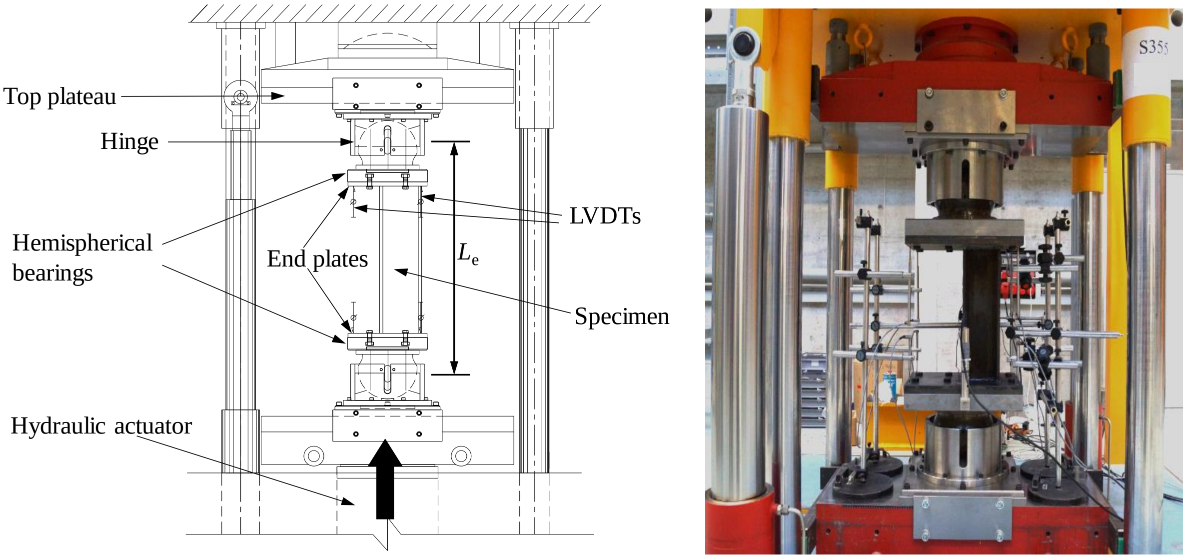

(a) Schematic diagram of test setup (b) Experimental setup

Fig.10. Testing configuration for specimens under combined loading

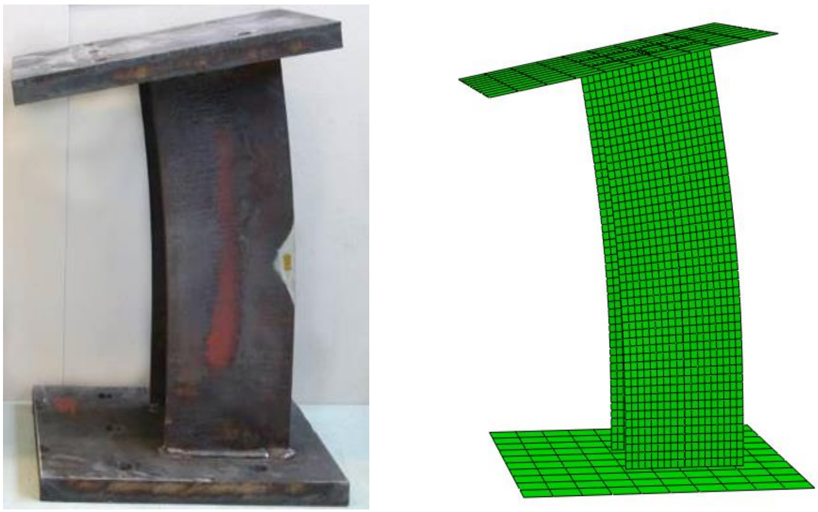

(a) Uniaxial bending plus compression (B5)

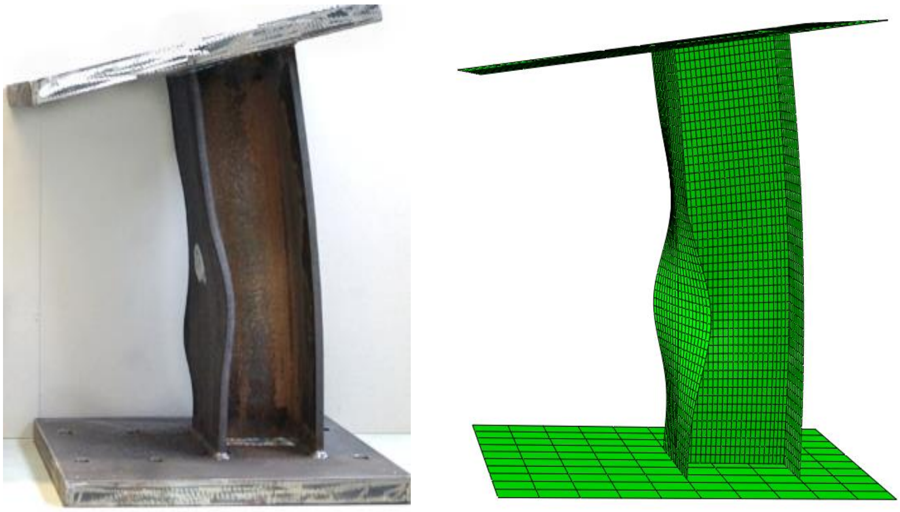

(b) Biaxial bending plus compression (B3)

Fig.11. Typical experimental and numerical failure modes from tests under combined loading

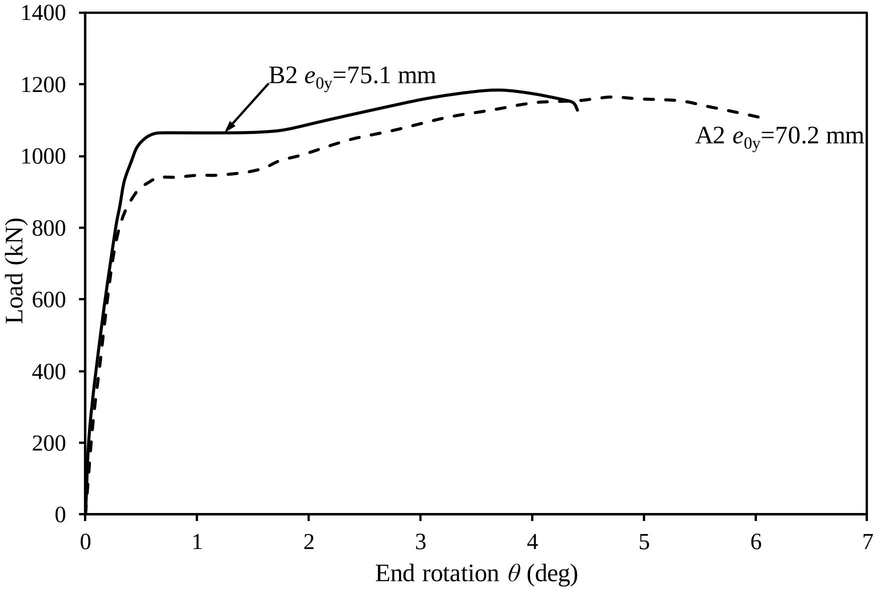

(a) Load-end rotation curves for specimens A2 and B2

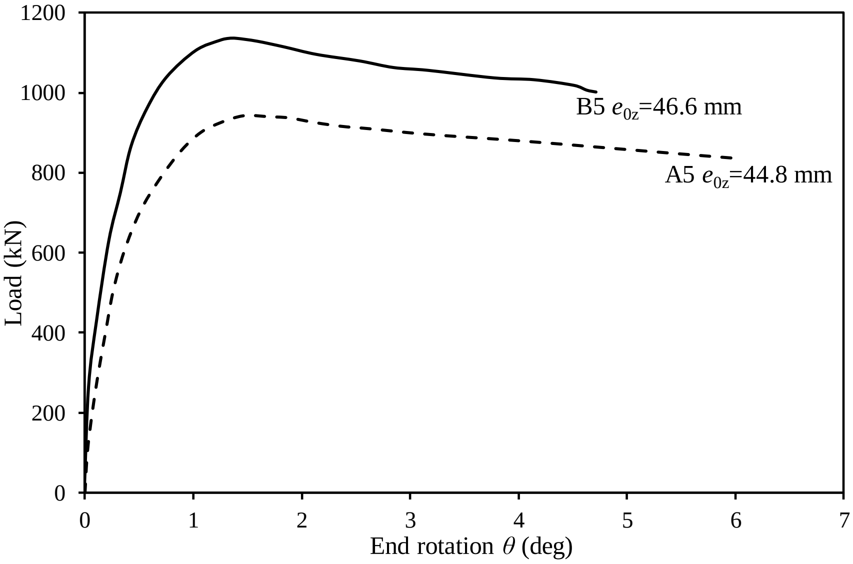

(b) Load-end rotation curves for specimens A5 and B5

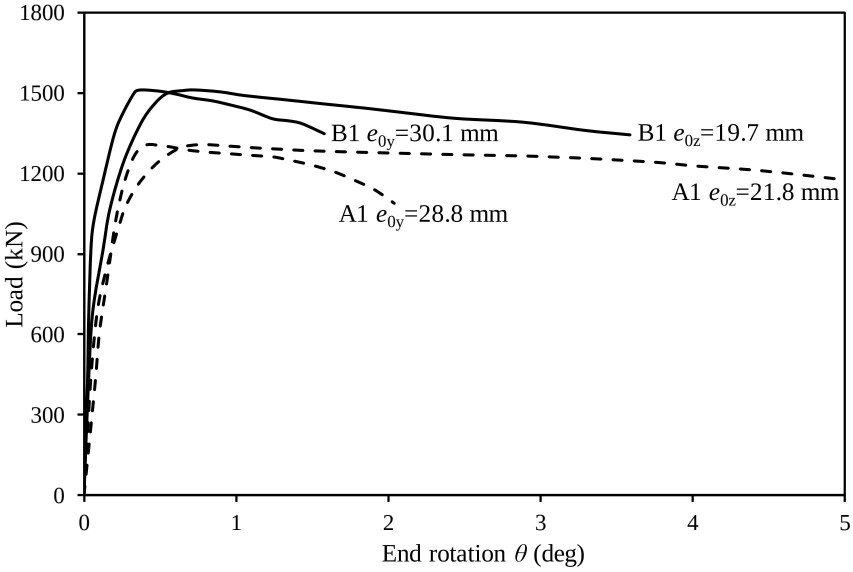

(c) Load-end rotation curves for specimens A1 and B1

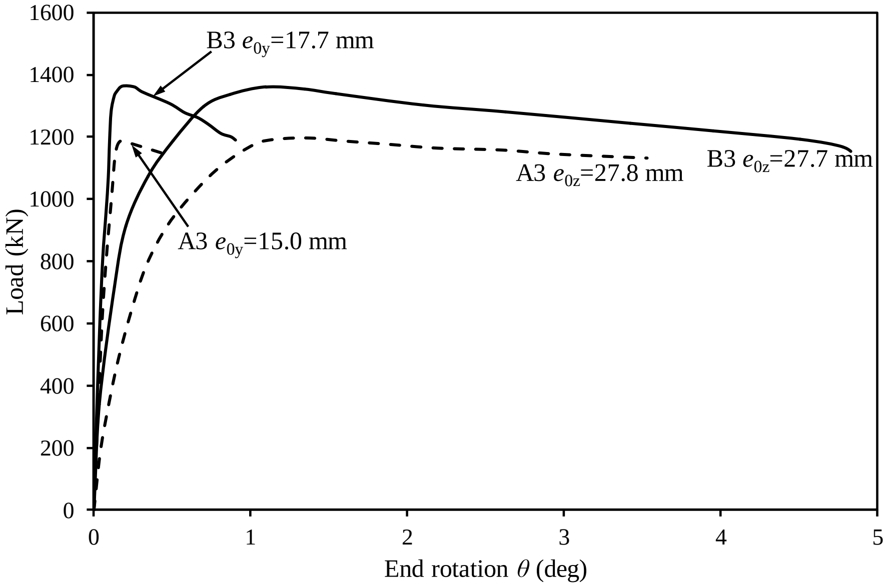

(d) Load-end rotation curves for specimens A3 and B3

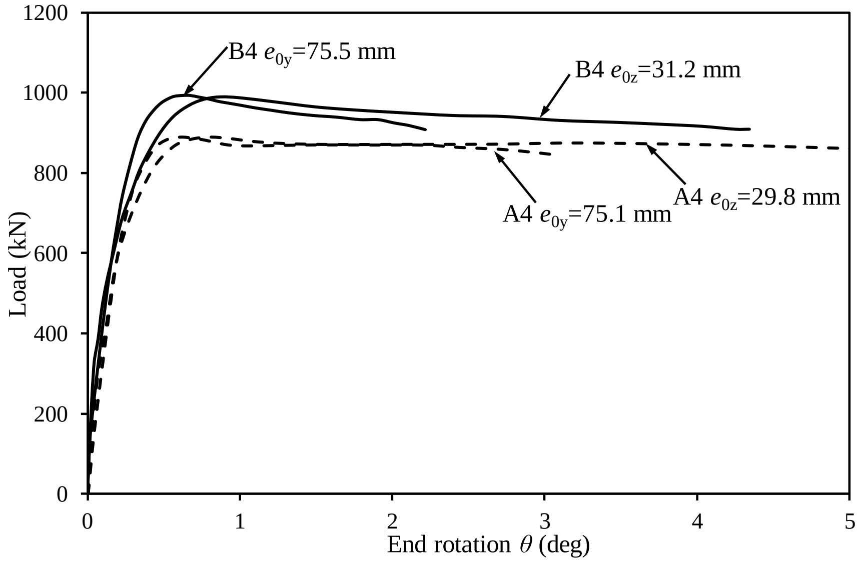

(e) Load-end rotation curves for specimens A4 and B4

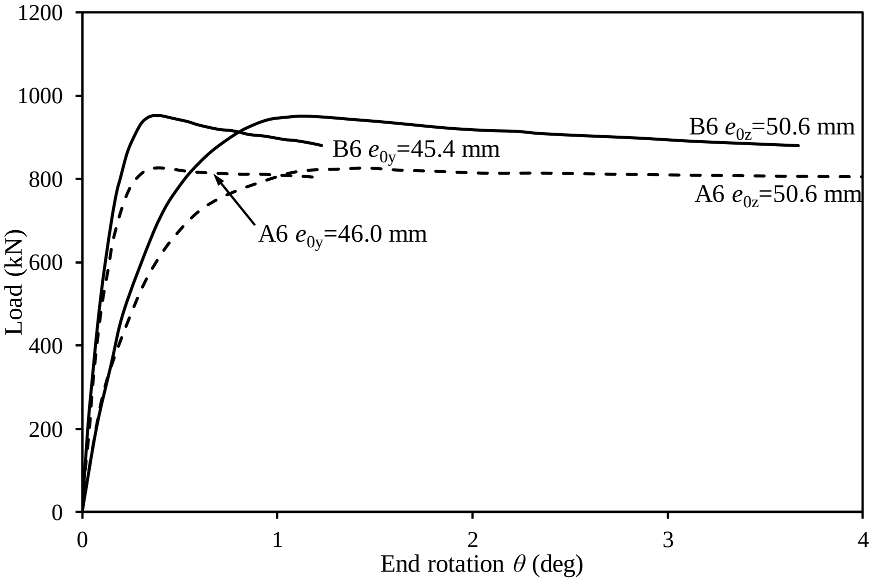

(f) Load-end rotation curves for specimens A6 and B6

Fig.12. Measured load-end rotation curves from combined loading tests

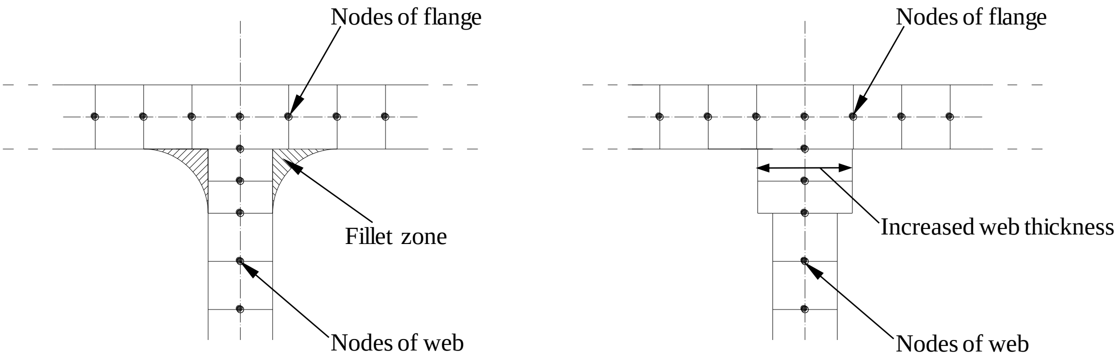

Fig.13. Representation of the fillet zones of I-sections in FE models

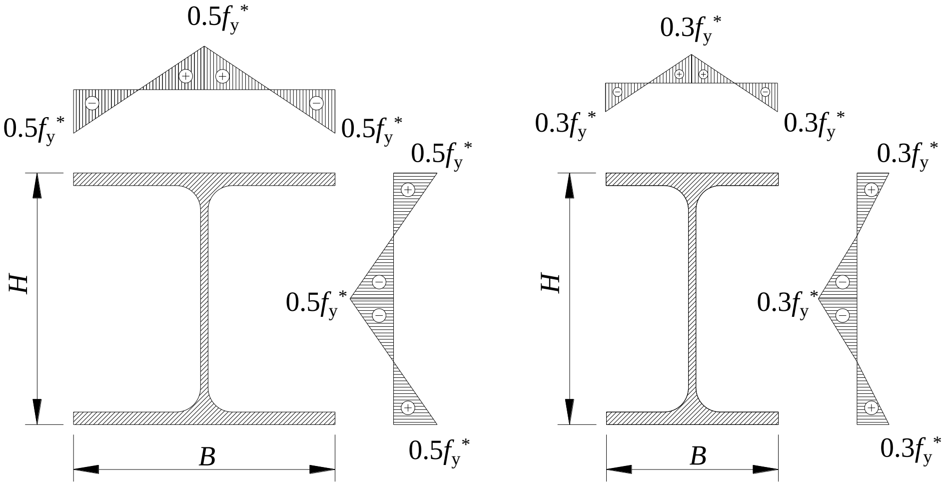

(a) $H/B \leq 1.2$ (b) $H/B > 1.2$

Fig.14. Residual stress patterns applied to FE models

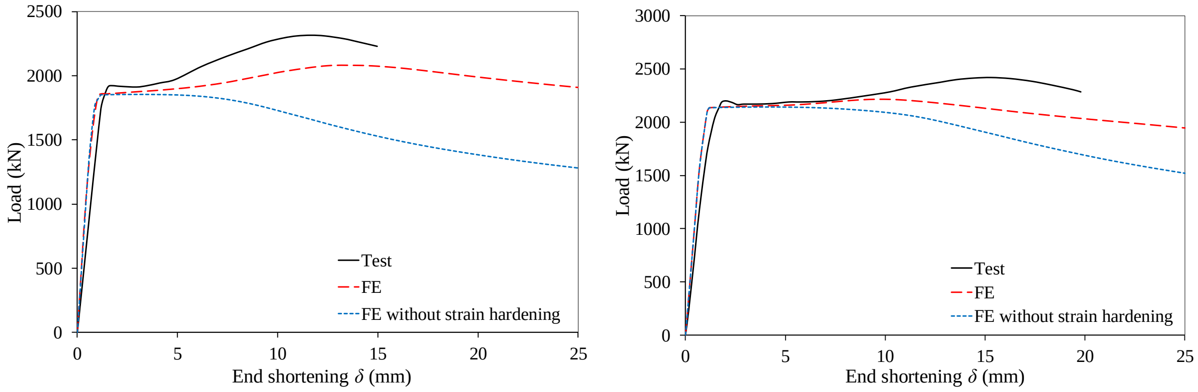

(a) A7 (b) B7

Fig.15. Experimental and numerical load-end shortening curves for stub column specimens

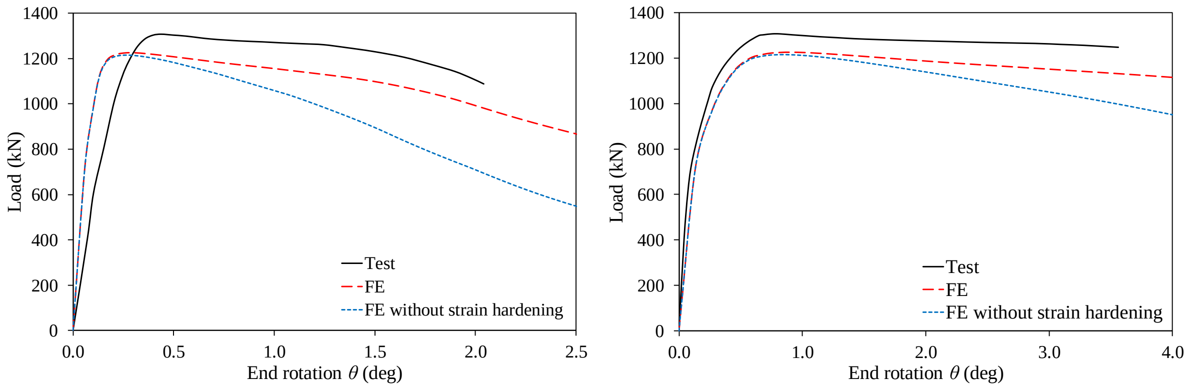

(a) A1 Major axis (e_{0y} = 28.8 mm) (b) A1 Minor axis (e_{0z} = 21.8 mm)

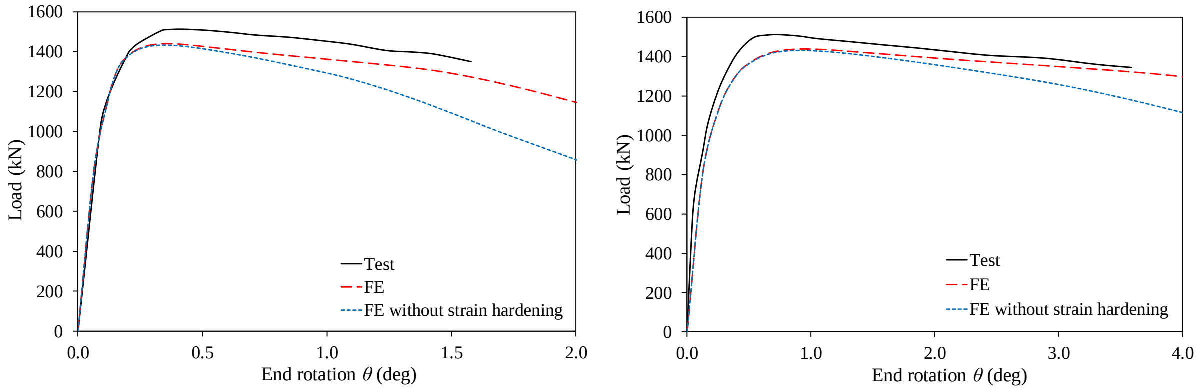

(c) B1 Major axis (e_{0y} = 30.1 mm) (d) B1 Minor axis (e_{0z} = 19.7 mm)

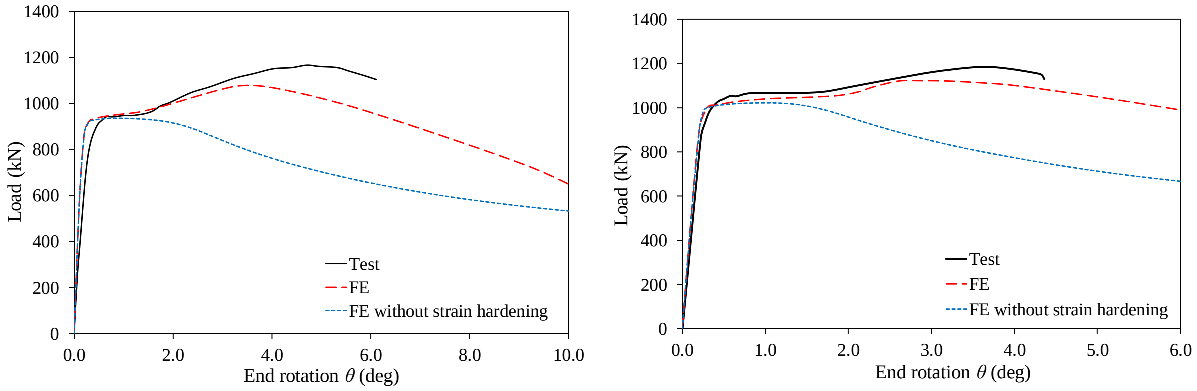

(e) A2 Major axis (e_{0y} = 70.2 mm) (f) B2 Major axis (e_{0y} = 75.1 mm)

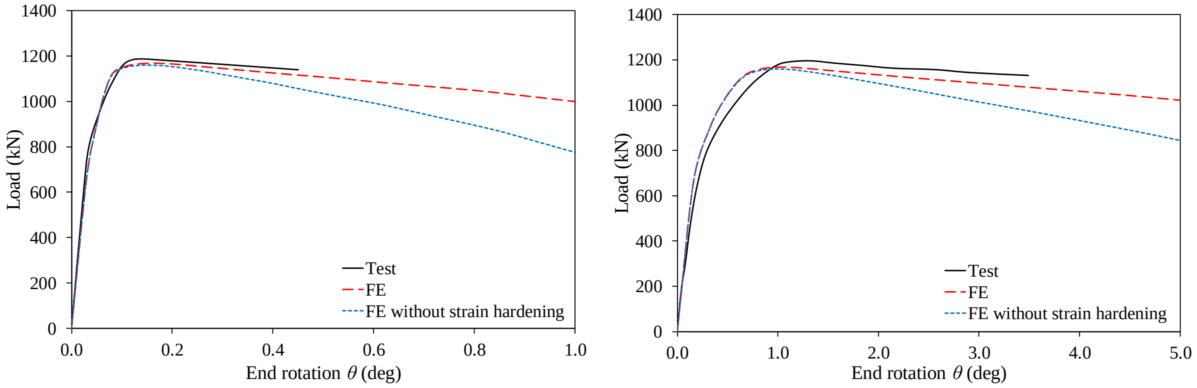

(g) A3 Major axis (e_{0y} = 15.0 mm) (h) A3 Minor axis (e_{0z} = 27.8 mm)

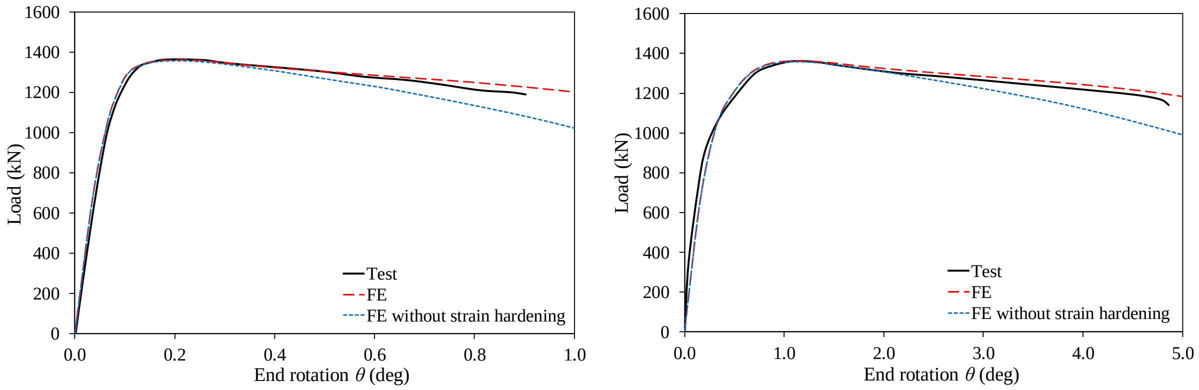

(i) B3 Major axis (e_{0y} = 17.7 mm) (j) B3 Minor axis (e_{0z} = 27.7 mm)

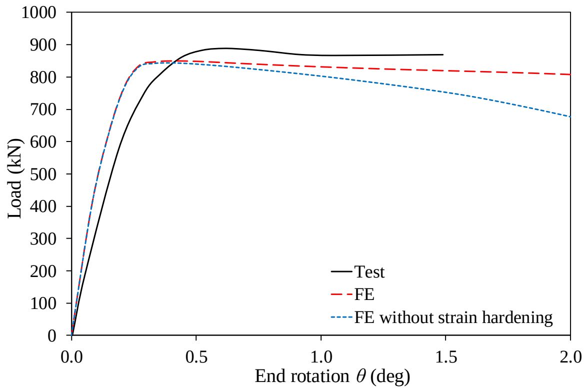

(k) A4 Major axis (e_{0y} = 75.1 mm) (l) A4 Minor axis (e_{0z} = 29.8 mm)

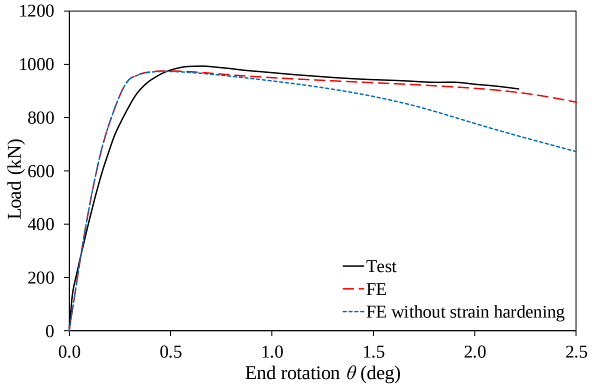

(m) B4 Major axis (e_{0y} = 75.5 mm) (n) B4 Minor axis (e_{0z} = 31.2 mm)

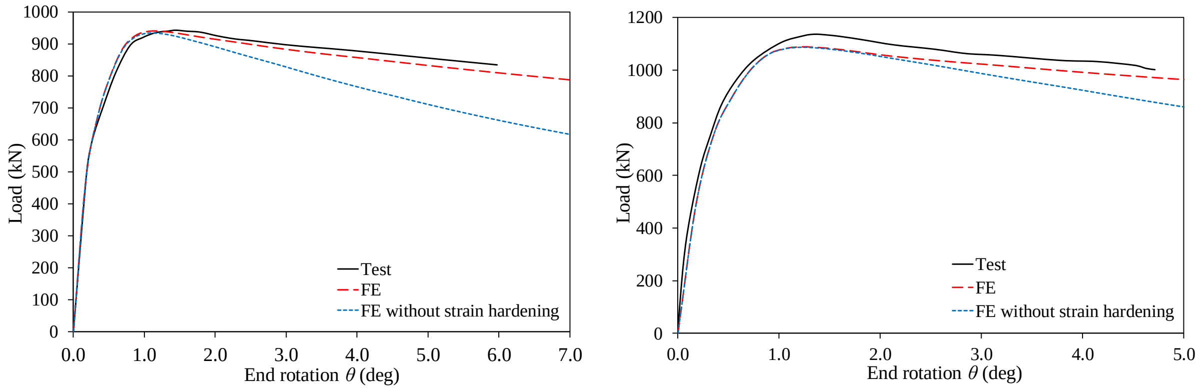

(o) A5 Minor axis (e_{0z} = 44.8 mm) (p) B5 Minor axis (e_{0z} = 44.6 mm)

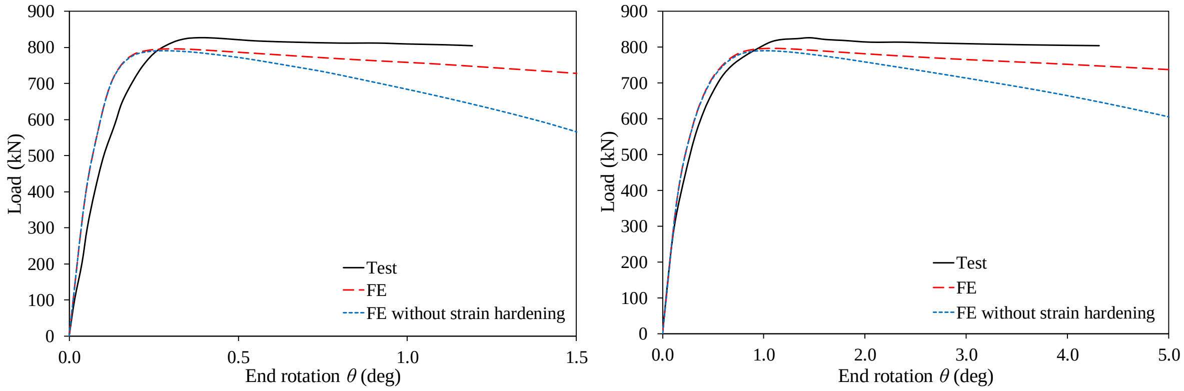

(q) A6 Major axis (e_{0y} = 46.0 mm) (r) A6 Minor axis (e_{0z} = 50.6 mm)

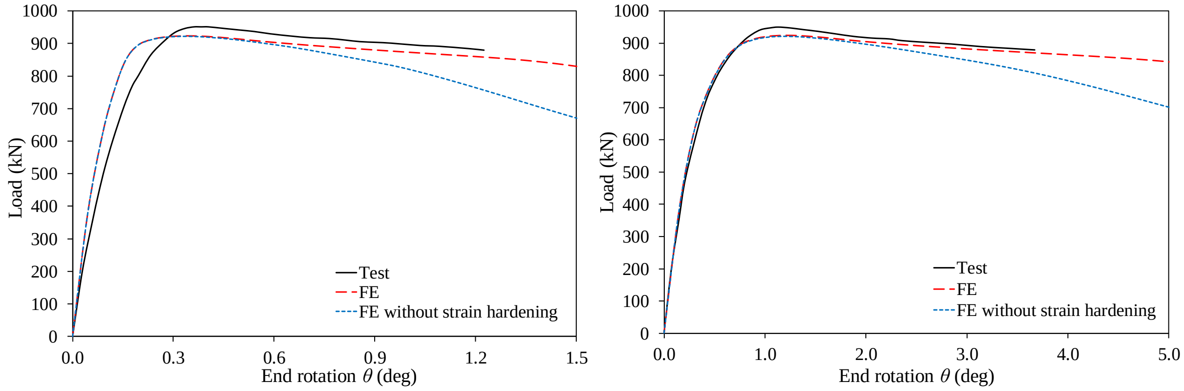

(s) B6 Major axis (e_{0y} = 45.4 mm) (t) B6 Minor axis (e_{0z} = 50.6 mm)

Fig.16. Experimental and numerical load-end rotation curves for biaxial bending plus compression tests

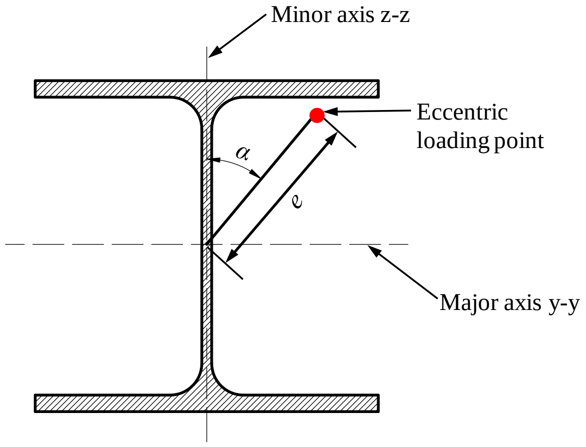

Fig.17. Definition of the loading eccentricity *e* and angle *α* in [12]